

# Electron beam expansion and deflection uncertainty for active spacecraft charging applications

Álvaro Romero-Calvo\* and Hanspeter Schaub †

*Department of Aerospace Engineering Sciences, University of Colorado Boulder, CO, United States.*

Gabriel Cano-Gómez‡

*Departamento de Física Aplicada III, Universidad de Sevilla, Sevilla, Spain.*

**Novel active sensing technologies have been recently proposed to measure the electrostatic potential and characterize non-cooperative objects in Geosynchronous Equatorial Orbit (GEO) and deep space. Such technologies make use of electron beams to excite the emission of secondary electrons and X-Rays and infer properties of the emitting surface. In this context, the quantification of the uncertainty in the landing position and energy of the beam becomes fundamental for future applications. This work presents a quasi-analytical, uncoupled, and computationally efficient electron beam expansion and deflection model designed to estimate the beam dynamics in scales of 10s of meters in GEO. The validity space of the model is explored in the ECLIPS Space Environments Simulation Facility in a worst-case scenario. The landing uncertainty in a representative two-spacecraft scenario is studied by means of Monte Carlo simulations, and a Fourier Amplitude Sensitivity Testing (FAST) Global Sensitivity Analysis (GSA) is finally run to determine the most influential inputs of the system.**

## I. Introduction

THE use of secondary electrons (SEE) [1] and X-rays [2, 3] has been recently proposed to touchlessly sense the electrostatic potential of objects in geosynchronous orbit or deep space. These methods, illustrated in Fig. 1, make use of a positively charged servicing craft that directs a high-energy electron beam at the object of interest such that low-energy secondary electrons and X-rays are emitted from the surface. The secondary electron flux is accelerated towards the servicing craft and arrives with an energy equal to the potential difference between the two bodies. The servicing craft measures the electron and photon energy spectrum and, knowing its own potential, infers the potential of the target [4]. This technology may find application in the electrostatic detumbling [5] and reorbiting [6–8] of debris, Coulomb formations, virtual structures, material identification, and the mitigation of arcing during rendezvous, docking, and proximity operations [9], among others. Potential levels of the order of 10s of keV and beam current levels of up to 1 mA are employed in these scenarios [10].

Many of the aforementioned applications rely on the accurate modeling of electron beam dynamics. Past missions have made use of electron beams in space, with some examples being SCATHA [11] or the Electron Drift Instruments at GEOS [12], Freja [13], Cluster [14], and MMS [15]. Particle simulation models have been employed to study the injection and long-term propagation of electron beams in plasma environments [16–20]. The applications here discussed, however, are limited to the *initial expansion* phase, where the beam density is much larger than the GEO plasma density and the expansion dynamics are driven by the radial electric field in the beam cross section [21]. In addition, beam dynamics are significantly affected by the electric fields from nearby charged bodies. This particular environment motivates the development of a simplified and computationally efficient analytical framework of analysis that decouples electron beam expansion and deflection.

The purpose of this paper is to quantify the deflection and dispersion of electron beams in active spacecraft charging scenarios. A quasi-analytical model is first built in Sec. II and contrasted with experimental results in Sec. III. The uncertainty in key parameters is quantified in Sec. IV, and the electron beam arrival to the target spacecraft is analyzed by means of Monte Carlo simulations assuming the perspective of the servicing spacecraft. The contribution of each

---

\*Graduate Research Assistant, Department of Aerospace Engineering Sciences, University of Colorado Boulder, CO, United States. AIAA student member. email:alvaro.romerocalvo@colorado.edu

†Professor, Glenn L. Murphy Chair in Engineering, Ann and H.J. Smead Aerospace Engineering Sciences, AIAA and AAS Fellow.

‡Professor, Departamento de Física Aplicada III, Universidad de Sevilla, Avenida de los Descubrimientos s/n, 41092, Sevilla, Spain.

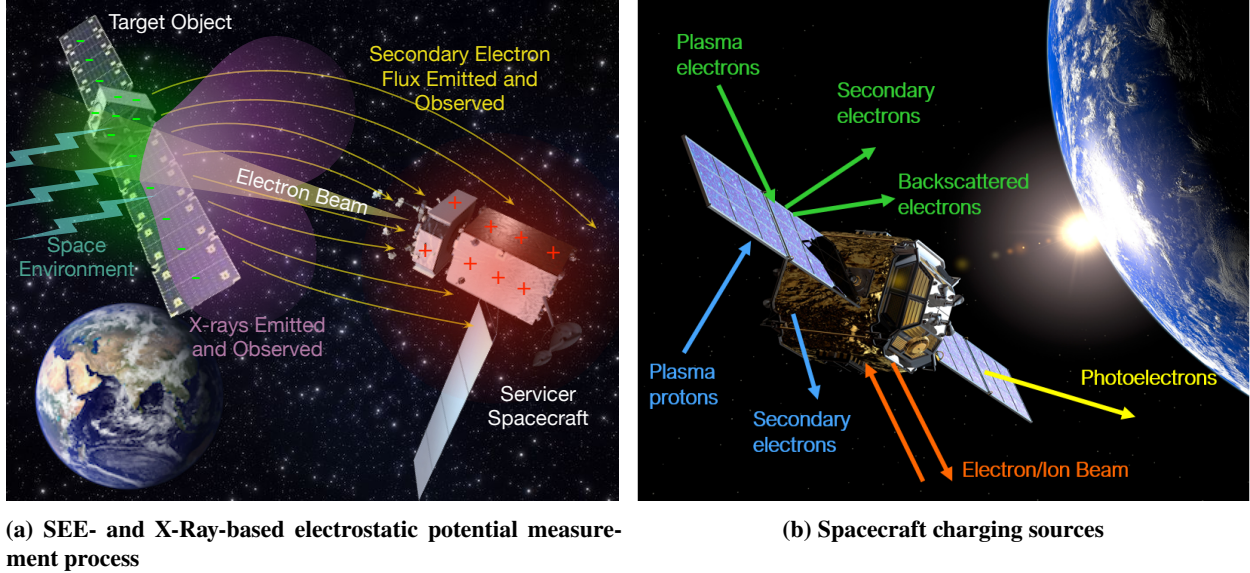


**Fig. 1** Conceptual representation of the spacecraft potential sensing and charge processes [1]

parameter to the uncertainty in the outputs is quantified with a FAST sensitivity analysis. Conclusions are finally given in Sec. V.

## II. Modeling

### A. Physical model

The propagation of electron beams in space is subject to several internal and external electromagnetic effects. The quasi-analytical physical model here presented assumes (i) a small beam deflection angle  $\theta$ , (ii) small radial expansion, (iii) axisymmetric distribution of geometry and loads within the beam cross-section, and (iv) negligible plasma interactions.

The first assumption is key for developing a computationally efficient simulation framework, as it decouples expansion and deflection problems. As explained in Sec. IV.A, small beam deflection angles are produced when the potential difference between servicer and target spacecrafts is significantly smaller than the electron beam energy. This is the case of interest for remote sensing applications; otherwise, the beam may never be able to hit the target. The second and third assumptions reduce the cross-section electrostatic surface integrals to one dimension by implementing an infinite cylindrical beam framework of analysis. Because the beam divergence angle rarely exceeds  $1^\circ$ , this is also appropriate. Finally, it is possible to discard plasma interactions, as their influence on the beam dynamics is negligible and spacecraft charging processes are not considered. Since the separation between servicer and target spacecrafts is of the order of 10s of meters, which represents a fraction of the GEO Debye length, the electron beam dynamics can be reasonably studied without taking into account complex plasma environments.

### B. Mathematical model

In the following framework, the deflection of the beam is assumed to be produced by the electromagnetic environment, while the expansion is consequence of the distribution of charge in the beam cross-section and the initial beam divergence angle. For both analyses, Lorentz's force defines the electromagnetic force on an electron through

$$\mathbf{F} = q(\mathbf{v} \times \mathbf{B} + \mathbf{E}), \quad (1)$$

with  $q$  and  $\mathbf{v}$  being the charge and velocity of the electron, and  $\mathbf{B}$  and  $\mathbf{E}$  denoting the magnetic flux density and electric field, respectively. The relativistic change in momentum of the particle is given by the balance

$$\frac{d(\gamma m_e \mathbf{v})}{dt} = \mathbf{F}, \quad (2)$$

where  $m_e$  is the mass of the electron,  $\gamma = (1 - \beta^2)^{-1/2}$ , with  $\beta = v/c$ , is the Lorentz factor, and the time derivative is inertial. The position  $\mathbf{x}$  in the inertial reference frame is computed as

$$\frac{d\mathbf{x}}{dt} = \mathbf{v}. \quad (3)$$

It should be noted that, in accordance with the special theory of relativity, the inertia of a particle with respect to a reference frame depends on its velocity magnitude with respect to such frame. Consequently, the term  $\gamma m_e$  defines the apparent mass of the particle.

For the sake of clarity, the *internal* fields are subsequently denoted by lowercase variables, while uppercase letters are associated with the *external* fields.

### 1. Expansion of cylindrical electron beams

The internal electromagnetic fields and forces generated by axisymmetric cylindrical beams can be approximated under the infinite length assumption. This leads to good estimates when the characteristic longitudinal (propagation) distance is much larger than the characteristic radius of the beam. If the force induced by the external electromagnetic field is approximately uniform in the beam cross-section, the internal forces determine the beam expansion rate.

Axisymmetric cylindrical beams generate radial electric and azimuthal magnetic fields. The first is readily derived from Gauss's law, resulting in [22]

$$\mathbf{e}(r, t) = \frac{q}{\epsilon_0 r} \int_0^r dr' n(r', t) r' \mathbf{u}_r, \quad (4)$$

where  $\epsilon_0$  is the permittivity of free space,  $n(r)$  denotes the volume density distribution of electrons, and  $\{\mathbf{u}_r, \mathbf{u}_\psi, \mathbf{u}_z\}$  describes a cylindrical reference system centered in the axis of the beam and whose  $z$  component is aligned with the velocity. Similarly, Ampère's law gives the azimuthal magnetic field [22]

$$\mathbf{b}(r, t) = \frac{\mu_0 q v_z(t)}{r} \int_0^r dr' n(r', t) r' \mathbf{u}_\psi, \quad (5)$$

with  $\mu_0$  being the permeability of free space, and  $v_z$  the propagation velocity of the beam (assumed to be uniform in the cross-section). The modules of the electric and magnetic fields are related through  $e = (c/\beta)b$ . By applying Eq. (1) to these fields the internal electromagnetic force becomes

$$\mathbf{f}(r, t) = \frac{q^2}{r\epsilon_0} (1 - \beta(t)^2) \int_0^r dr' n(r', t) r' \mathbf{u}_r, \quad (6)$$

where  $z$  component of the force, cause by the radial expansion velocity, has been neglected. The magnetic and electric forces are related through  $F_{\text{mag}} = -\beta^2 F_{\text{el}}$ . For relativistic electron beams, both terms are approximately compensated ( $\beta \rightarrow 1$ ), allowing long-distance transport at high current levels [22, 23].

The initial beam velocity profile is obtained in two steps. First, the velocity of propagation  $v_z(0)$  is computed from the initial relativistic kinetic energy,  $T = (\gamma - 1)m_0c^2$ , by solving for  $\gamma$  and  $\beta$ . Then, the initial divergence angle  $\delta$  is imposed as

$$\mathbf{v}(r, 0) \approx \frac{r\delta}{R_b} v_z(0) \hat{\mathbf{r}} + v_z(0) \hat{\mathbf{z}}, \quad (7)$$

where it is assumed that  $\delta \ll 1$  (quasi-collimated beam). This divergence angle is not caused by the electromagnetic repulsion between particles, but by the optical configuration of the electron gun itself. The initial electron density function,  $n(r, 0)$ , can be modeled as a finite quasi-Gaussian distribution defined by the electron beam current intensity  $I_b$ , energy  $E$ , and radius  $R_b$ . The condition

$$\int_0^{R_b} dr' 2\pi r' n(r', t) = \frac{I}{qv_z(t)}, \quad (8)$$

is then imposed at each time step to conserve the electron beam current. This expression assumes a uniform  $v_z$  component computed in a plane perpendicular to the axis of the beam, which is consistent with the low-expansion assumption of the model.

It should be noted that, although Eqs. 4-8 are given as a function of time (describing the movement of a particle), they are actually associated with a steady-state solution. Time is related to the arc parameter  $s$  along the beam centroid through  $s = v_z t$ . In a straight beam,  $s = z$ , and each of these expressions can be written in terms of the cylindrical coordinates  $r$  and  $z$ . The ratio  $\beta(t)$  also changes depending on the acceleration induced by external forces to the beam propagation velocity.

## 2. Deflection of cylindrical electron beams

The deflection of the beam is here identified with the trajectory of the centroid of the cross-section, which is driven by the external electric and magnetic fields. While the first is mainly produced by the potential difference between both spacecrafts, the second is imposed by the magnetic environment.

The charge  $q$  of a conducting body is related to its capacitance through  $q = V/C$ , where  $V$  is the potential. If  $V$  is known, then the capacitance can be used to determine charge distribution, from which the electric field can be directly computed. However, objects in close proximity will exhibit mutual capacitance effects [24], which must be accounted for to accurately determine the total charge on each of them. The Multi-Sphere Method (MSM) approximates the distribution of electric charge on a conducting body (for example, the conducting surface of a spacecraft) by means of charged spheres [25]. Given the potential on each sphere and its location relative to the rest, it is possible to analytically compute the charge from

$$\begin{pmatrix} V_1 \\ V_2 \\ \vdots \\ V_n \end{pmatrix} = k_c \begin{bmatrix} 1/R_1 & 1/r_{1,2} & \dots & 1/r_{1,n} \\ 1/r_{2,1} & 1/R_2 & \dots & 1/r_{2,n} \\ \vdots & \vdots & \ddots & \vdots \\ 1/r_{n,1} & 1/r_{n,2} & \dots & 1/R_n \end{bmatrix} \begin{pmatrix} Q_1 \\ Q_2 \\ \vdots \\ Q_n \end{pmatrix}, \quad \mathbf{V} = [S]\mathbf{Q}, \quad (9)$$

where  $[S]$  denotes the elastance matrix [24], which is also the inverse of the capacitance matrix, and  $k_c = 1/(4\pi\epsilon_0)$ . Assuming an equipotential spacecraft surface, the condition of electrostatic equilibrium in conducting bodies imposes that all  $V_i$  must be equal. This assumption is appropriate for a GEO spacecraft as the design specifications require the satellite to be built with all outer surfaces being electrically connected to avoid differential charging. The electric field  $\mathbf{E}$  is computed as the superposition of the one produced by each individual charge  $q_j$ , given by

$$\mathbf{E}_j(\mathbf{r}) = \frac{q_j}{4\pi\epsilon_0 r^3} \mathbf{r}, \quad r \geq r_j, \quad (10)$$

where  $\mathbf{r}$  denotes the radial position vector, and  $r_j$  is the radius of the sphere. The MSM method is predicated on the knowledge of the object's capacitance. An arbitrary number of spheres can be placed and their radii adjusted to match the capacitance of the MSM to the true value. Capacitance is a function of the object's geometry; however, analytic solutions are available for only a limited number of shapes (such as spheres or round plates). Therefore, a numerical scheme must be used to find the capacitance of the spacecraft. The Method of Moments is generally employed for that purpose [26].

This work assumes an arbitrarily oriented GEO magnetic field of 100 nT. Its large characteristic length of variation ( $\approx 10^3$  km), the small characteristic time of the beam deflection process ( $\approx 10^{-6}$  s), and the small influence of the field in the problem under consideration justify its treatment as a fixed parameter.

## 3. Nondimensional formulation

The numerical conditioning of the electron beam expansion and deflection problem can be largely improved by employing a dimensionless formulation of Eqs. 1-3, which become

$$\mathcal{F} = (\mathbf{v} \times \mathcal{B} + \mathcal{E}), \quad (11)$$

$$\frac{d(\gamma\mathbf{v})}{d\tau} = \mathcal{F}, \quad (12)$$

$$\frac{d\mathbf{x}}{d\tau} = \mathbf{v}, \quad (13)$$

where

$$\mathbf{x} = \frac{\mathbf{x}}{x_{\text{ref}}}, \quad \tau = \frac{t}{t_{\text{ref}}}, \quad \mathbf{v} = \frac{t_{\text{ref}}}{x_{\text{ref}}} \mathbf{v}, \quad \mathcal{B} = \frac{q_{\text{ref}} t_{\text{ref}}}{m_{\text{ref}}} \mathbf{B}, \quad \mathcal{E} = \frac{q_{\text{ref}} t_{\text{ref}}^2}{m_{\text{ref}} x_{\text{ref}}} \mathbf{E}, \quad \mathcal{F} = \frac{t_{\text{ref}}^2}{m_{\text{ref}} x_{\text{ref}}} \mathbf{F}. \quad (14)$$

The electron mass and charge are taken as a reference ( $m_{\text{ref}}, q_{\text{ref}}$ ), with the characteristic time being  $t_{\text{ref}} = 10^{-6}$  s. The characteristic length  $x_{\text{ref}}$  denotes the initial electron beam radius  $R_b$  and the mean spacecraft separation  $L_{\text{ref}}$  for the expansion and deflection problems, respectively. In other words, two different dimensionless problems are solved simultaneously.

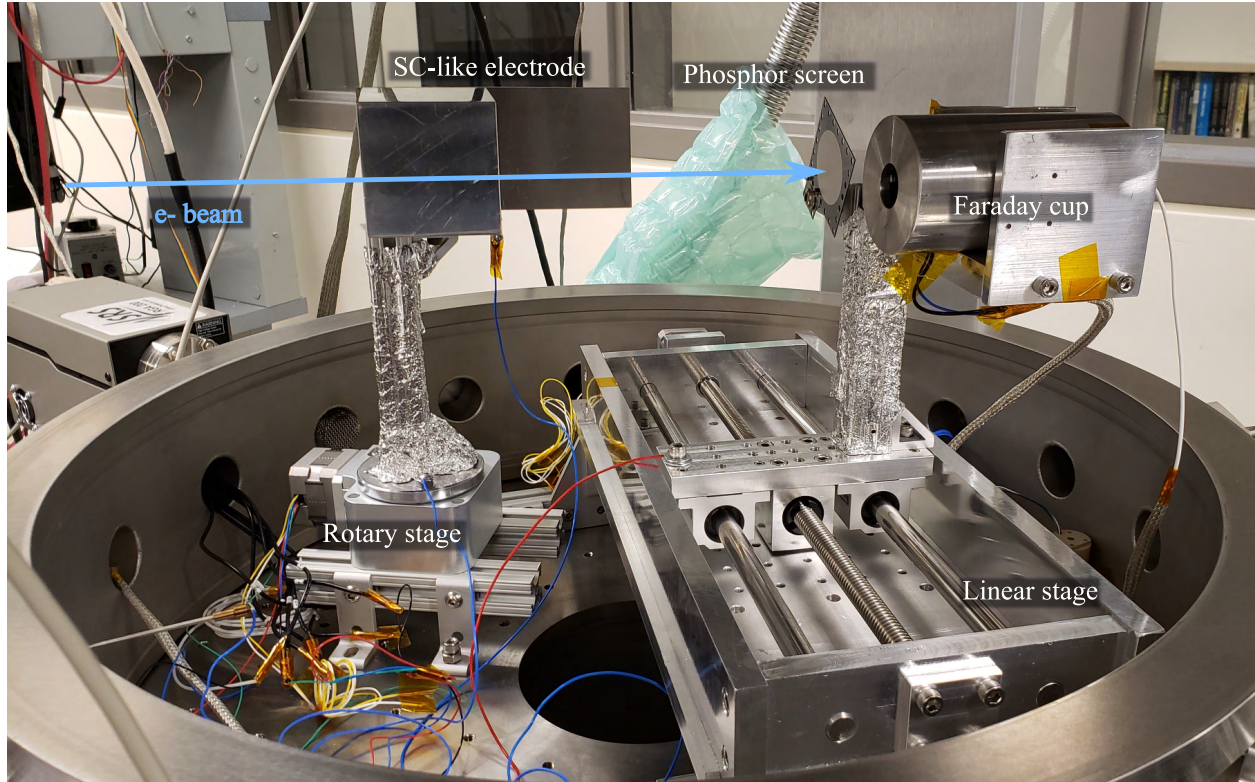


**Fig. 2** Experimental setup inside the ECLIPS chamber

#### 4. Validity metric

As noted in Sec. II.A, the analytical model introduced in this section remains valid while the beam deflection angle

$$\theta = \arccos \left[ \frac{\mathbf{v}(0) \cdot \mathbf{v}(t_f)}{|\mathbf{v}(0)| |\mathbf{v}(t_f)|} \right], \quad (15)$$

remains small, with  $t_f$  denoting the final simulation time. The additional dimensionless parameter

$$\mathcal{R} = \frac{\gamma m v^2}{|qL(\mathbf{v} \times \mathbf{B} + \mathbf{E})_{\perp}|} = \frac{\gamma v^2}{|(\mathbf{v} \times \mathfrak{B} + \mathfrak{E})_{\perp}|} \quad (16)$$

is defined to describe the ratio between the instantaneous electromagnetic gyroradius and the characteristic spacecraft separation  $L_{\text{ref}}$ , with  $\perp$  denoting the external force component in the beam cross-section and the different variables referring to the deflection problem. The metric  $\mathcal{R}$  shows how different beam locations are affected by the electromagnetic environment. Provided that  $\theta \ll 1$  and  $\mathcal{R} \gg 1$ , this framework of analysis should give accurate approximations of the solution.

### III. Analysis of validity metrics

The model presented in Sec. II relies on a number of assumptions that limit its validity space. However, provided that such assumptions are met, a computationally efficient and powerful analysis tool is obtained. With the purpose of exploring the performance of the model in a worst-case scenario, the experimental setup shown in Fig. 2 is tested in the ECLIPS Space Environment Simulation Facility [27]. The assembly exposes an electron beam from a Kimball Physics EMG-4212D electron gun to the electric field generated by a charged spacecraft-like electrode mounted on a rotary stage. The shape and location of the beam spot at approximately 35 cm from the gun orifice are observed with a 3.81 cm diameter rugged phosphor screen, and the spatial distribution is obtained with a Faraday cup mounted on a linear stage. The beam is configured at 1 keV energy and 10  $\mu\text{A}$  current, while the electrode is set at -100 to -500 V employing a

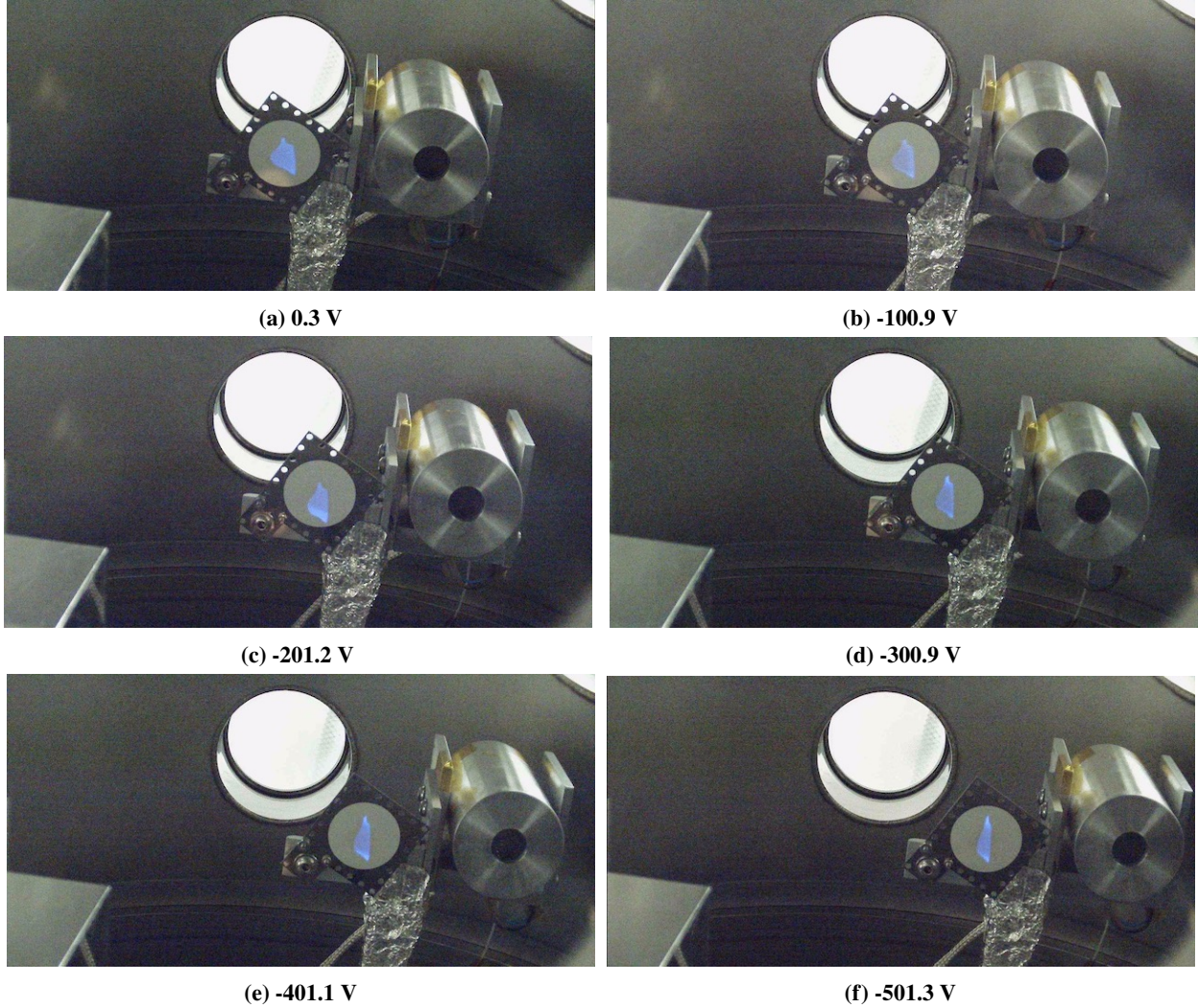


**Fig. 3 Electron beam spot in the phosphor screen under different electrode potentials**

Matsusada AU-30R1 high-voltage power supply. The electron flux at the Faraday cup is measured with a Keithley 2400 multimeter. Finally, the system is automated by means of a LabView VI interface.

Figure 3 shows the beam spot profiles at the phosphor screen for -100 to -500 V. Because the gun orifice is slightly below the symmetry plane of the electrode, a voltage decrease leads to a slight downwards deflection. This is compensated with a fine tuning of the vertical gun deflection settings, which do not alter the horizontal position or shape of the spot. Figure 3a shows a  $\approx 13$  mm diameter beam cross-section, which is considerably larger than the initial  $\approx 3$  mm diameter beam. Since the shape remains unaltered for different beam current intensities, it can be concluded that the expansion is not induced by the electrostatic repulsion between electrons, but by the initial velocity spread angle  $\delta$ . As the voltage decreases, the beam is deflected away from the electrode and its cross-section is elongated vertically. The spot shape differs significantly from the 0 V case below -300 V, indicating the existence of small gyro radii with  $\mathcal{R} \approx 1$ . These observations are complemented with the electron flux distribution in Fig. 4, where the narrowing process reduces the width of the flux peak and its amplitude. Based on the 0 V case, the spread angle can be estimated as  $\delta \approx 2.5^\circ$ . It should be noted that the apparent beam radius shown in Fig. 3a is smaller than the one reported in Fig. 4. This is due to limitations imposed by the power density threshold of the phosphor screen and the effective aperture of the Faraday cup\*.

The influence of the electrode rotation angle  $\alpha$  on the beam deflection and spot shape is also explored in Fig. 5 for

\*The variations in light intensity at the phosphor screen are caused by the unwanted Electron-Beam-Induced-Deposition (EBID) of carbon and heavy molecules over the surface, and not by variations in the distribution of electrons in the beam cross-section.

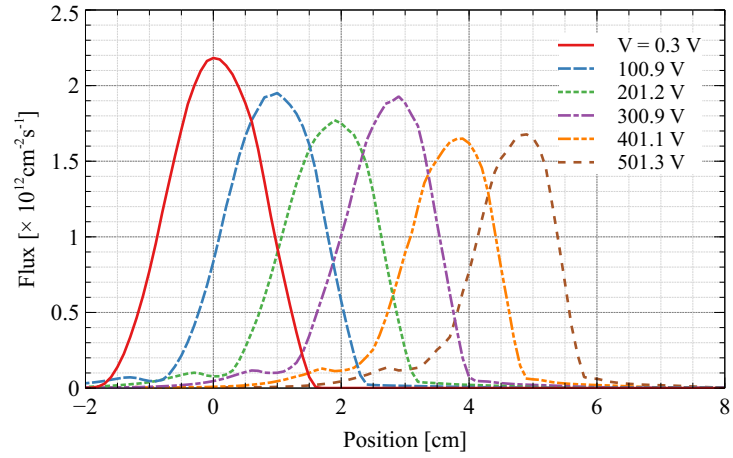


**Fig. 4** Experimental electron flux distribution as a function of the applied electrode potential

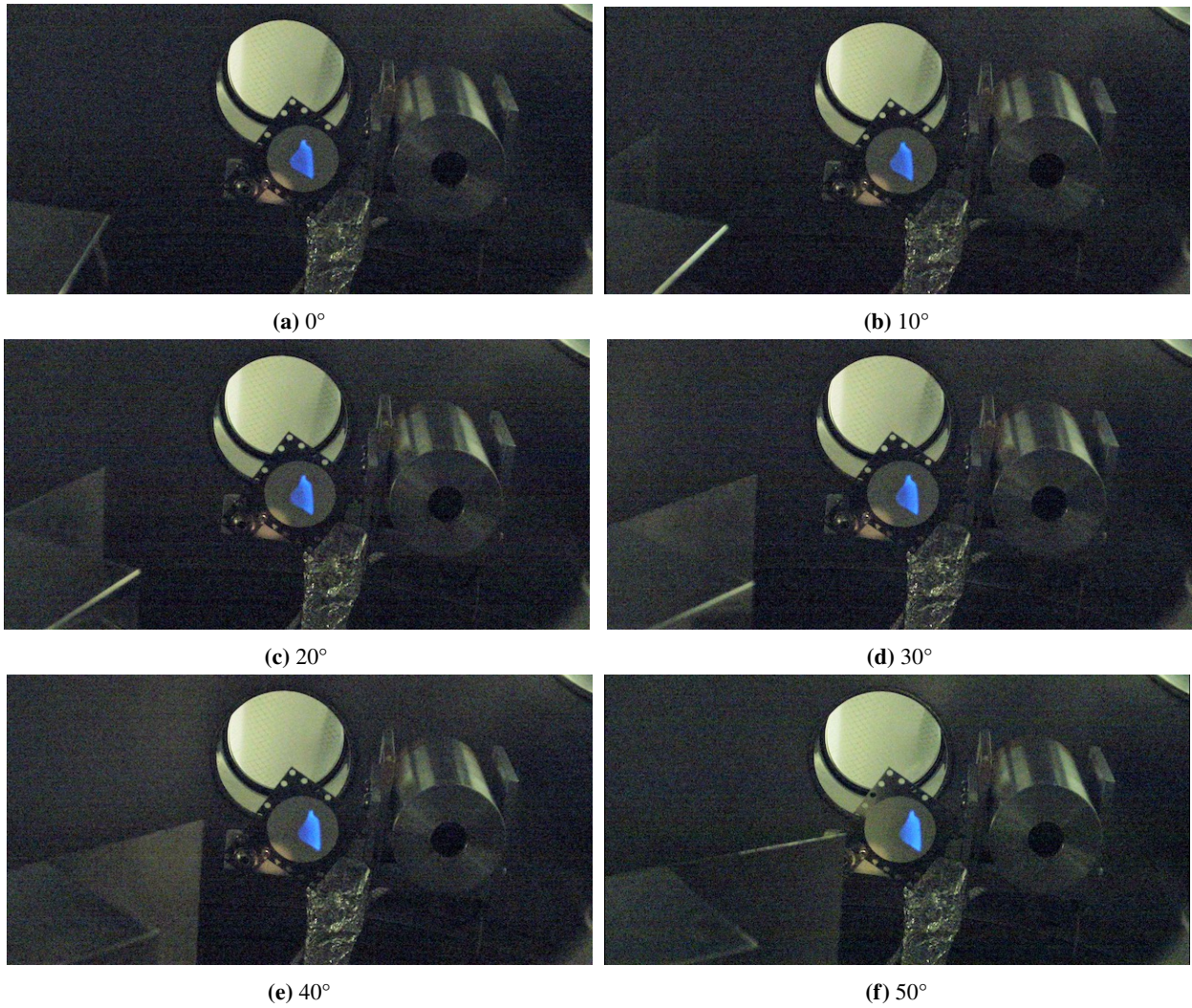


**Fig. 5** Electron beam spot in the phosphor screen under different electrode rotation angles at -100 V

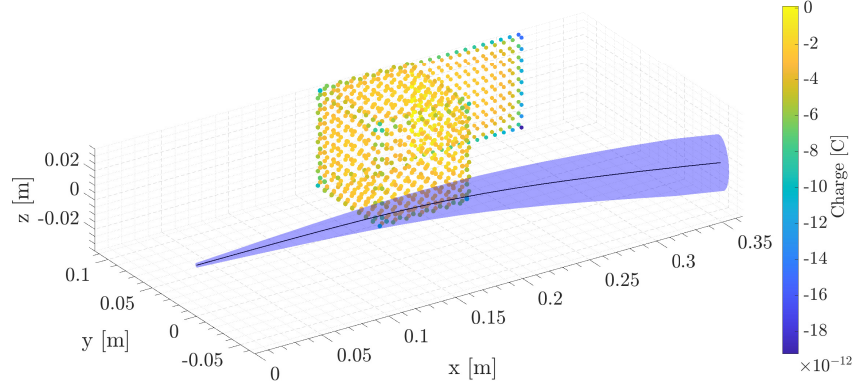


**Fig. 6 MSM representation of the experimental setup with electron beam propagation at -500 V**

$V = -100$  V and  $\alpha = 10^\circ$  to  $50^\circ$ . Although the beam is deflected and the cross section is modified, these effects are much less pronounced than in Fig. 3.

The model introduced in Sec. II is not designed to predict the elongation of the beam cross-section, but will still give accurate estimations for those cases where the beam deflection angle is small. In order to evaluate the validity metrics defined in Sec. II.B.4, the experimental setup is reproduced with a 934-spheres MSM representation of the spacecraft-like electrode. The setup is shown in Fig. 2 for an electrode potential of -500 V, that corresponds to the case in Fig. 3f, and a beam expansion angle  $\delta = 2.5^\circ$ . The validity metrics  $\mathcal{R}$  and  $\theta$  are reported in Fig. 7 as a function of the electrode potential  $V$  and rotation angle  $\alpha$ . An increase in the electrode potential decreases the minimum  $\mathcal{R}$  value and increases the deflection angle  $\theta$ , reaching  $\approx 3$  and  $9.5^\circ$  for -300 V, respectively. Larger values lead to significant beam cross-section deformations, as shown in Figs. 3e-3f. Similarly, the rotation of the electrode creates a second minimum in the  $\mathcal{R}$  plot (i.e. a second maximum in the electromagnetic force), but since this minimum is larger than in the -200 V case, its effects on the beam cross-section are less noticeable. Due to the large beam expansion angle  $\delta$ , the magneto-electrostatic repulsion between electrons plays virtually no role the expansion dynamics of the beam. This is in agreement with experimental observations.

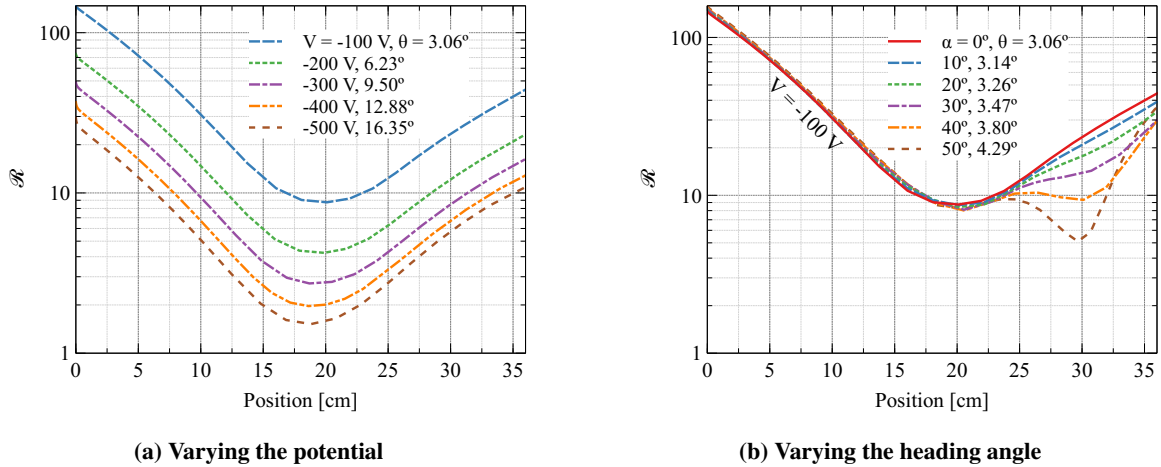


**Fig. 7 Validation metrics  $\mathcal{R}$  and  $\theta$  as a function of the electrode potential and heading angle**

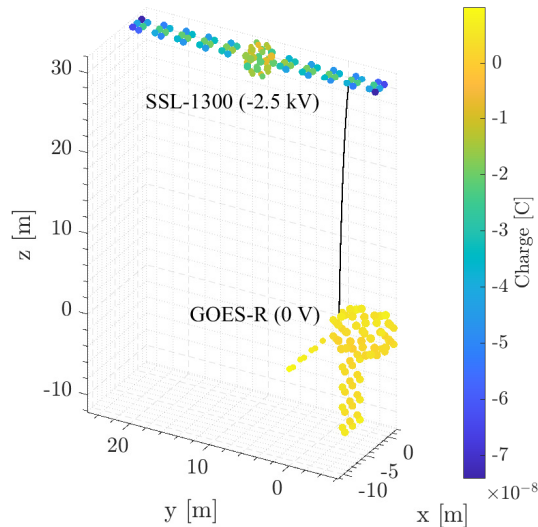


**Fig. 8** Geometry of the 2-SC problem for the basic simulation parameters (see Table 1). The red line represents the displacement of the  $e^-$  beam centroid.

## IV. Uncertainty in beam dynamics

### A. Active charging scenario

Once the validity of the beam model has been contrasted with experimental observations, the base scenario of analysis is introduced in Fig. 8. The GOES-R<sup>†</sup> and SSL-1300<sup>‡</sup> spacecraft MSM models are shown together with the  $e^-$  beam centroid evolution. The servicer spacecraft (0 V) is positively charged with respect to the target (-2.5 kV), generating a net electrostatic force that tends to deflect and slow down the 5 keV, 10  $\mu$ A electrons from  $4.2 \cdot 10^7$  m/s to  $3.2 \cdot 10^7$  m/s. The electron beam energy must be larger than the absolute potential difference to allow the electrons to reach the target surface. The  $\mathcal{R}$  parameter depends quadratically on the propagation speed and approximately linearly on the beam energy (see Eq. (16)), and hence the physical model here adopted is particularly well suited for high beam energy cases.

The trade-off between beam energy and spacecraft potentials is analyzed in Fig. 9a by comparing the validation metrics along the beam trajectory in three different scenarios. As expected, an increase in beam energy leads to larger  $\mathcal{R}$  and smaller  $\theta$  values, while a decrease in the target spacecraft potential has the opposite effect. In the nominal case ( $E_b = 5$  keV,  $V = -2.5$  kV), a deflection angle  $\theta = 5.33^\circ$  and a minimum  $\mathcal{R} = 4$  are reached, satisfying the validity range of the model. These values are analogous to the experimental -200 V case depicted in Fig. 3c and analyzed in Fig. 7.

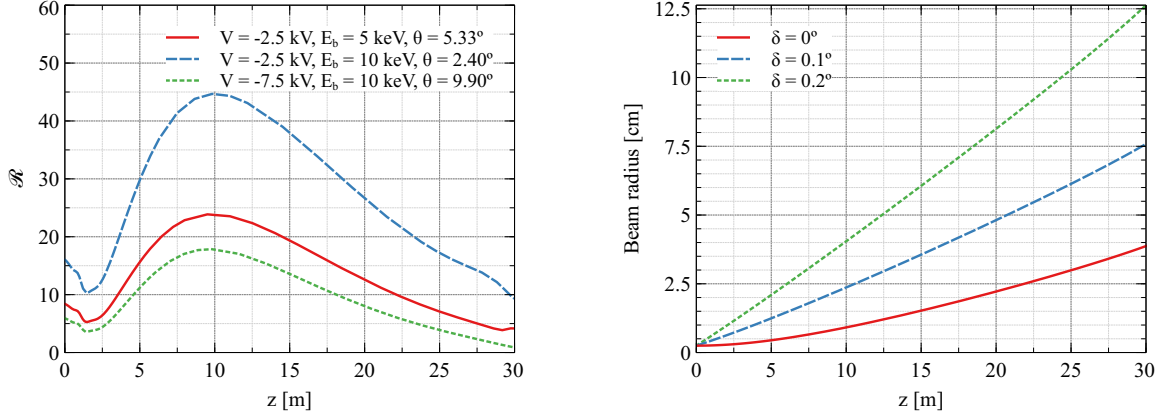
Figure 9b explores the beam expansion dynamics for different deflection angles. When a stream of collimated electrons ( $\delta = 0$ ) exit the gun, the magneto-electrostatic repulsion expands the beam radius from 2.5 to 40 mm in the 30 m flight. The trajectory of those electrons is non-linear, but as the initial  $\delta$  angle is increased, a linear expansion is achieved. This qualitatively different behavior unveils the existence of *repulsive* and *inertial* expansion regimes. Because the magneto-electrostatic repulsion is negligible in the inertial scenario, future versions of the model described in Sec. II may benefit from a switching metric between different frameworks of analysis.

### B. Uncertainty quantification analysis

The model built in Sec. II is employed to quantify the uncertainty in the position of the beam in an active spacecraft charging scenario. The analysis is designed from the perspective of a servicing spacecraft that needs to direct the beam at a particular area of the target. A total of 702 uncertain variables are considered, with 688 being associated to the MSM spheres that approximate the charge distribution of the two-spacecraft system. The list of variables and their

<sup>†</sup><https://www.goes-r.gov/spacesegment/spacecraft.html> (Consulted on: 11/28/2020)

<sup>‡</sup>[http://sslmda.com/html/1300\\_series\\_platform.php](http://sslmda.com/html/1300_series_platform.php) (Consulted on: 11/28/2020)



(a) Validation metrics  $\mathcal{R}$  and  $\theta$  as a function of the target spacecraft potential  $V$  and beam energy  $E_b$  (b) Beam radius evolution as a function of divergence angle

**Fig. 9 Validation metrics and beam radius evolution for nominal spacecraft charging scenario**

distribution is detailed in Table 1. The outputs of the analysis are (i) the radius of the beam cross section at the end of flight, (ii) the centroid landing position in the target plane, which is perpendicular to the line of sight between both spacecrafts, (iii) the landing energy, and (iv) the time of flight.

Due to the large number of parameters and reduced computational cost of the simulation, a Monte Carlo analysis is preferred over other uncertainty quantification methods. The relative influence of each input parameter on the output metrics is measured by means of sensitivity indices, computed with a Fourier Amplitude Sensitivity Testing (FAST) suite from Ref. 28<sup>§</sup>.

### C. Results

A Monte Carlo analysis is carried out with  $10^4$  random realizations generated from the distributions in Table 1. Each simulation takes approximately 0.6 s after parallelizing the code with 7 CPU threads. The solution converges in mean and variance for both the expansion and deflection problems.

<sup>§</sup><https://www.mathworks.com/matlabcentral/fileexchange/40759-global-sensitivity-analysis-toolbox> (Consulted on: 11/30/2020)

**Table 1 Uncertainty analysis parameters**

Variable	Distribution	Mean	STD	Unit
Beam current ( $I_b$ )	Normal	10	0.1	$\mu\text{A}$
Beam energy ( $E_b$ )	Normal	5	0.05	keV
Initial divergence angle ( $\delta$ )	Uniform	0.1	Lims: [0, 0.2]	deg
Initial particle density STD ( $\sigma_b$ )	Normal	0.83	0.083	mm
Servicer potential ( $V_{\text{ser}}$ )	Normal	0	0.05	kV
Servicer, Euler-313 ( $\psi_{\text{ser}}, \theta_{\text{ser}}, \phi_{\text{ser}}$ )	Normal	[0,90,0]	[0.1,0.1,0.1]	deg
Target potential ( $V_{\text{tar}}$ )	Normal	-2.5	0.25	kV
Target, Euler-313 ( $\psi_{\text{tar}}, \theta_{\text{tar}}, \phi_{\text{tar}}$ )	Normal	[0,180,0]	[5,5,5]	deg
Relative Position ( $r_x, r_y, r_z$ )	Normal	[0,10,32]	[0.5,0.5,1]	m
Capacitances (x172)	Normal	Dataset	1%	C
Spheres pos. (x516)	Normal	Dataset	1%	m
Initial beam radius	Fixed	2.5	0	mm

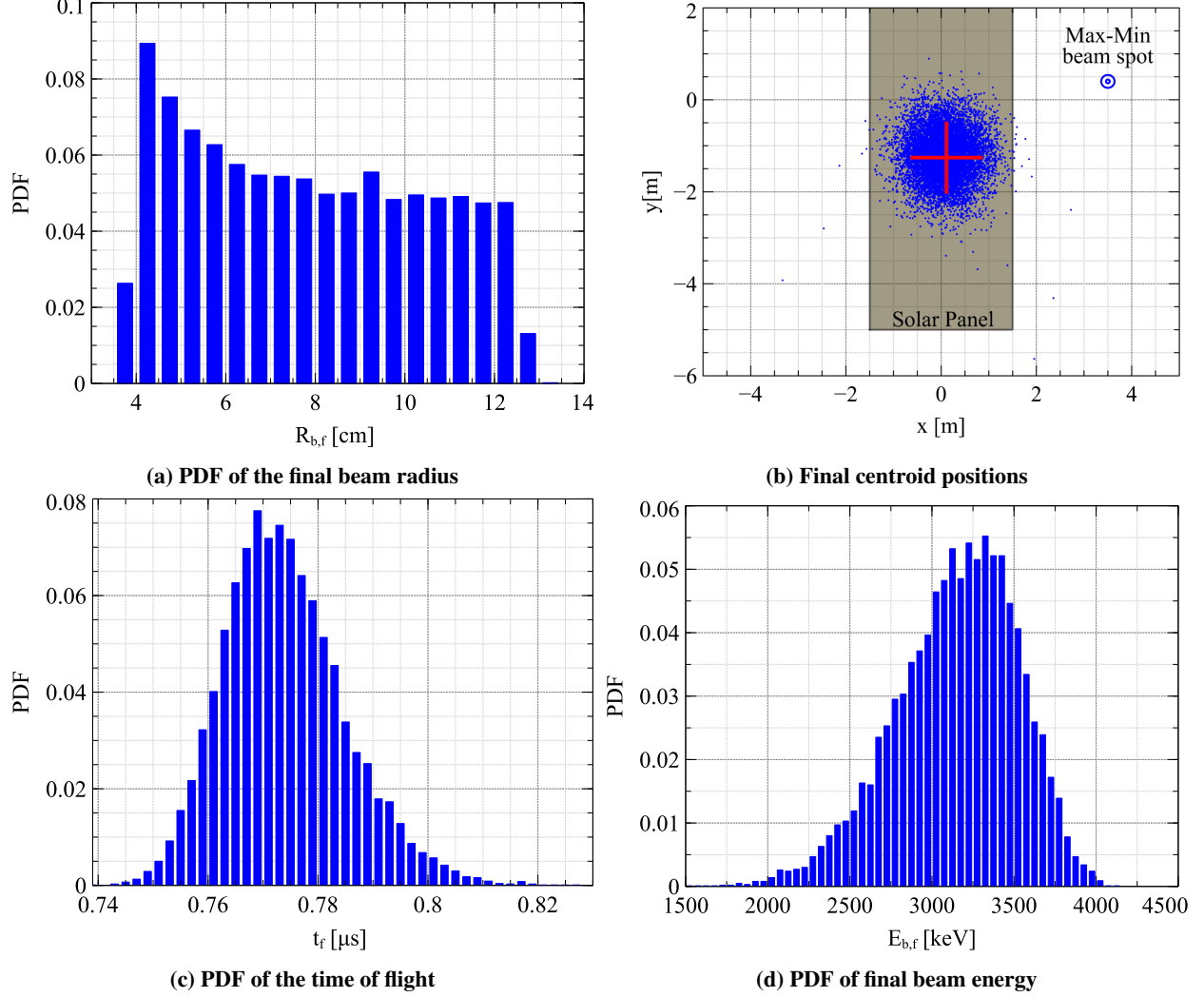


**Fig. 10** Result of the Monte Carlo simulation

Results in Fig. 10 show the Probability Density Functions (PDFs) of the model outputs: (a) final beam radius  $R_{b,f}$ , (b) final centroid position  $p_{x,f}$  and  $p_{y,f}$ , (c) time of flight  $t_f$ , and (d) final beam energy  $E_{b,f}$ . The first follows a quasi-uniform distribution, clearly influenced by the uniform sampling of the initial deflection angle  $\delta$ , and spans from 4 to 13 cm. These expansion values, computed for  $\delta \subseteq [0, 0.2]$ , are small in comparison with the spread of the beam centroid shown in Fig. 10b, where the target  $[0.11, -1.26]$  m is marked as a red cross. The landing positions follow a multi-Gaussian distribution with mean  $\mu = [0.07, -1.20]$  and covariance  $C = [0.20, -0.006; -0.006, 0.28]$ . This implies that the beam centroid has a 93.9% probability of intercepting the SSL-1300 solar panel, represented as a rectangle in the figure, while the chances of hitting a 20 cm diameter circle surrounding the target are just a 0.3%. The time of flight PDF is represented in Fig. 10c and follows a lognormal distribution with logarithmic mean  $\mu = -14.07$  and variance  $\sigma^2 = 2.14 \cdot 10^{-4}$ . This result can be relevant for applications employing pulsed beam modulations to filter the returning secondary electron flux from the target. Finally, the landing energy PDF is shown in Fig. 10d and fitted with a Weibull distribution (scale 3309.98, shape 9.97) with mean  $\mu = 3148.55$  and variance  $\sigma^2 = 144294$ . The landing energy determines the secondary electron yield, and is hence important for the remote potential sensing technologies described in previous works [1].

In order to determine the influence of each input on the outcomes reported in Fig. 10, a Fourier Amplitude Sensitivity Testing (FAST) Global Sensitivity Analysis (GSA) is conducted. The analysis is limited to the 15 non-MSM inputs in Table 1 to minimize its computational cost. Although 688 MSM variables are removed, Table 2 shows how the total variances remain practically identical, denoting that such uncertain inputs have a negligible effect in the final

**Table 2 Comparison of output variances between the full 702 parameters and the reduced 15 parameters MC analyses**

	$V(R_{b,f})$ [m <sup>2</sup> ]	$V(p_{x,f})$ [m <sup>2</sup> ]	$V(p_{y,f})$ [m <sup>2</sup> ]	$V(E_{b,f})$ [keV <sup>2</sup> ]	$V(t_f)$ [s <sup>2</sup> ]
<b>Full</b>	6.830e-4	0.204	0.276	1.387e5	1.301e-16
<b>Reduced</b>	6.790e-4	0.203	0.269	1.456e5	1.319e-16

distributions.

Table 2 reports the sensitivity coefficients for  $10^4$  realizations. The five model outputs (final beam radius  $E_{b,f}$ , positions  $p_{x,f}$  and  $p_{y,f}$ , energy  $E_{b,f}$ , and time of flight  $t_f$ ) are listed in the rows, while the inputs are shown in the columns. Bold fonts are employed to highlight the largest sensitivities, showing that each output variance can be mainly explained with less than two inputs. For instance, the final beam radius is mainly dependent on the initial divergence angle, while the final positions are related to their corresponding uncertainties in the relative spacecraft position vector.  $p_{y,f}$  is also dependent on the target potential because it promotes the divergence of the beam (experimentally observed in Fig. 3). Although the results seem to point out that the variance in  $p_{x,f}$  is also explained by the beam current  $I_b$ , this should be attributed to numerical errors, because expansion and deflection problems are uncoupled. The final beam energy  $E_{b,f}$  and time of flight  $t_f$  are mainly dependent on the initial beam energy  $E_b$  and target spacecraft potential  $V_{tar}$ , which explain different percentages of the variance due to the different uncertainty bands in Table 1. The attitude of each spacecraft does not explain the variance in any output variable; however, this is caused by the small attitude disturbance angles selected in Table 1, which will likely increase with less accurate attitude determination sensors.

## V. Conclusions

The accurate modeling of short-term electron beam dynamics in active spacecraft charging scenarios is key for the development of novel electrostatic potential sensing technologies. In this paper, a computationally efficient quasi-analytical model is introduced that decouples the beam expansion and deflection problems. Experimental observations in space-like environment show that this framework of analysis is appropriate for quasi-cylindrical beams under small deflection angles, supporting its utilization in several problems of interest.

A servicing spacecraft application that directs an electron beam towards a target object at 30 m in GEO is investigated to analyze the beam pointing uncertainty. The sensitivity of the beam dynamics to a set of input parameters is studied by means of Monte Carlo simulations with  $10^4$  realizations. Although the electron beam centroid is shown to hit the target spacecraft with 93.85% probability, this happens within a large 3 m  $\pm 3\sigma$  Gaussian interval around the target. The beam radius is at most 13 cm for this particular scenario, but may be modified by changing the initial dispersion angle. A FAST sensitivity analysis is run to determine which input parameters explain the variance in the final metrics, showing that the relative spacecraft position and target spacecraft potential account for most of the variance. Similarly, the final electron beam energy and time of flight uncertainties depend mostly on the beam energy and target potential distributions. Future space systems dealing with accurate beam pointing and narrow landing energy requirements should consequently minimize the uncertainty in those parameters.

**Table 3 Normalized sensitivity indices from FAST sensitivity analysis with 15 inputs and 5 outputs. The values are scaled by a factor of 10 for convenience.**

	$I_b$	$E_b$	$\sigma_b$	$V_{tar}$	$V_{ser}$	$r_x$	$r_y$	$r_z$	$\phi_{tar}$	$\theta_{tar}$	$\psi_{tar}$	$\phi_{ser}$	$\theta_{ser}$	$\psi_{ser}$	$\delta$
$R_{b,f}$	0.053	0.112	0.011	0.306	0.044	0.009	0.019	0.121	0.005	0.001	0.015	0.056	0.318	0.365	<b>8.563</b>
$p_{x,f}$	<b>1.208</b>	0.204	0.009	0.016	0.004	<b>8.284</b>	0.001	0.003	0.233	0.002	0.005	0.002	0.025	0.002	0.002
$p_{y,f}$	0.004	0.030	0.033	<b>1.550</b>	0.354	0.003	<b>7.888</b>	0.109	0.001	0.003	0.001	0.003	0.020	0.001	0.001
$E_{b,f}$	0.056	<b>1.541</b>	0.021	<b>7.122</b>	0.554	0.071	0.126	0.226	0.117	0.138	0.006	0.005	0.005	0.013	0.001
$t_f$	0.028	<b>3.524</b>	0.005	<b>4.661</b>	0.760	0.006	0.024	0.741	0.010	0.238	0.001	0.000	0.001	0.001	0.001

## Acknowledgments

The authors thank Prof. Alireza Doostan for his assistance in the development of the uncertainty quantification analysis, and Dr. Miles Bengtson and Kieran Wilson for fruitful discussions on the setup and operation of the vacuum chamber experiment. This work was partially supported by U.S. Air Force Office of Scientific Research under grant FA9550-20-1-0025 and the *la Caixa* Foundation (ID 100010434), under agreement LCF/BQ/AA18/11680099.

## References

- [1] Bengtson, M. T., Wilson, K. T., and Schaub, H., “Experimental Results of Electron Method for Remote Spacecraft Charge Sensing,” *Space Weather*, Vol. 18, No. 3, 2020, pp. 1–12.
- [2] Wilson, K., and Schaub, H., “X-Ray Spectroscopy for Electrostatic Potential and Material Determination of Space Objects,” *IEEE Transactions on Plasma Science*, Vol. 47, No. 8, 2019, pp. 3858–3866.
- [3] Wilson, K. T., Bengtson, M. T., and Schaub, H., “X-ray Spectroscopic Determination of Electrostatic Potential and Material Composition for Spacecraft: Experimental Results,” *Space Weather*, Vol. 18, No. 4, 2020, pp. 1–10.
- [4] Bengtson, M., Hughes, J., and Schaub, H., “Prospects and Challenges for Touchless Sensing of Spacecraft Electrostatic Potential Using Electrons,” *IEEE Transactions on Plasma Science*, Vol. 47, No. 8, 2019, pp. 3673–3681.
- [5] Casale, F., Schaub, H., and Biggs, J. D., “Lyapunov Optimal Touchless Electrostatic Detumbling of Geostationary Debris Using Surface Multisphere Models,” *AIAA Journal of Spacecraft and Rockets*, 2020. *Under Review*.
- [6] Hughes, J., and Schaub, H., “Prospects of Using a Pulsed Electrostatic Tractor With Nominal Geosynchronous Conditions,” *IEEE Transactions on Plasma Science*, Vol. 45, No. 8, 2017, pp. 1887–1897.
- [7] Bengtson, M., Wilson, K., Hughes, J., and Schaub, H., “Survey of the electrostatic tractor research for reorbiting passive GEO space objects,” *Astrodynamics*, Vol. 2, No. 4, 2018, pp. 291–305.
- [8] Hughes, J. A., and Schaub, H., “Electrostatic Tractor Analysis Using a Measured Flux Model,” *Journal of Spacecraft and Rockets*, Vol. 57, No. 2, 2020, pp. 207–216.
- [9] Wilson, K., and Schaub, H., “Predictive Control For Spacecraft Proximity Operations Under Electrostatic Perturbations,” *Proceedings of the IEEE Aerospace Engineering Conference, Big Sky, Montana*, 2021.
- [10] Schaub, H., and Moorero, D. F., “Geosynchronous Large Debris Reorbiter: Challenges and Prospects,” *The Journal of the Astronautical Sciences*, Vol. 59, No. 1, 2012, pp. 161–176.
- [11] Olsen, R., and Cohen, H., “Electron beam experiments at high altitudes,” *Advances in Space Research*, Vol. 8, No. 1, 1988, pp. 161 – 164.
- [12] Melzner, F., Metzner, G., and Antrack, D., “The GEOS electron beam experiment,” *Space Science Instrumentation*, Vol. 4, 1978, pp. 45–55.
- [13] Paschmann, G., Boehm, M., Höfner, H., Frenzel, R., Parigger, P., Melzner, F., Haerendel, G., Kletzing, C. A., Torbert, R. B., and Sartori, G., “The Electron Beam Instrument (F6) on Freja,” *Space Science Reviews*, Vol. 70, No. 3, 1994, pp. 447–463.
- [14] Paschmann, G., Melzner, F., Frenzel, R., Vaith, H., Parigger, P., Pagel, U., Bauer, O. H., Haerendel, G., Baumjohann, W., Scopke, N., Torbert, R. B., Briggs, B., Chan, J., Lynch, K., Morey, K., Quinn, J. M., Simpson, D., Young, C., McIlwain, C. E., Fillius, W., Kerr, S. S., Mahieu, R., and Whipple, E. C., “The Electron Drift Instrument for Cluster,” *Space Science Reviews*, Vol. 79, No. 1, 1997, pp. 233–269.
- [15] Torbert, R. B., Vaith, H., Granoff, M., Widholm, M., Gaidos, J. A., Briggs, B. H., Dors, I. G., Chutter, M. W., Macri, J., Argall, M., Bodet, D., Needell, J., Steller, M. B., Baumjohann, W., Nakamura, R., Plaschke, F., Ottacher, H., Hasiba, J., Hofmann, K., Kletzing, C. A., Bounds, S. R., Dvorsky, R. T., Sigsbee, K., and Kooi, V., “The Electron Drift Instrument for MMS,” *Space Science Reviews*, Vol. 199, No. 1, 2016, pp. 283–305.
- [16] Okuda, H., and Berchem, J., “Injection and propagation of a nonrelativistic electron beam and spacecraft charging,” *Journal of Geophysical Research: Space Physics*, Vol. 93, No. A1, 1988, pp. 175–195.
- [17] Okuda, H., and Ashour-Abdalla, M., “Propagation of a nonrelativistic electron beam in three dimensions,” *Journal of Geophysical Research: Space Physics*, Vol. 95, No. A3, 1990, pp. 2389–2404.

- [18] Okuda, H., and Ashour-Abdalla, M., “Injection of an overdense electron beam in space,” *Journal of Geophysical Research: Space Physics*, Vol. 95, No. A12, 1990, pp. 21307–21311.
- [19] Winglee, R. M., “Simulations of pulsed electron beam injection during active experiments,” *Journal of Geophysical Research: Space Physics*, Vol. 96, No. A2, 1991, pp. 1803–1817.
- [20] Koga, J., and Lin, C. S., “A simulation study of radial expansion of an electron beam injected into an ionospheric plasma,” *Journal of Geophysical Research: Space Physics*, Vol. 99, No. A3, 1994, pp. 3971–3983.
- [21] Gendrin, R., “Initial expansion phase of an artificially injected electron beam,” *Planetary and Space Science*, Vol. 22, No. 4, 1974, pp. 633 – 636.
- [22] Humphries, S., *Charged Particle Beams*, Wiley, 1990. Chapter 5: Introduction to Beam-Generated Forces.
- [23] Lewellen, J. W., Buechler, C. E., Carlsten, B. E., Dale, G. E., Holloway, M. A., Patrick, D. E., Storms, S. A., and Nguyen, D. C., “Space-Borne Electron Accelerator Design,” *Frontiers in Astronomy and Space Sciences*, Vol. 6, 2019, p. 35.
- [24] Smythe, W., *Static and Dynamic Electricity*, 3<sup>rd</sup> ed., McGraw–Hill, 1968.
- [25] Stevenson, D., and Schaub, H., “Multi-Sphere Method for modeling spacecraft electrostatic forces and torques,” *Advances in Space Research*, Vol. 51, No. 1, 2013, pp. 10 – 20.
- [26] Hughes, J. A., and Schaub, H., “Heterogeneous Surface Multisphere Models Using Method of Moments Foundations,” *Journal of Spacecraft and Rockets*, Vol. 56, No. 4, 2019, pp. 1259–1266.
- [27] Wilson, K., Bengston, M., Maxwell, J., Romero-Calvo, A., and Schaub, H., “Characterization of the ECLIPS Space Environments Simulation Facility,” *Proceedings of the 2021 AIAA SciTech Forum and Exposition*, 2021.
- [28] Cannavó, F., “Sensitivity analysis for volcanic source modeling quality assessment and model selection,” *Computers & Geosciences*, Vol. 44, 2012, pp. 52 – 59.